Journal of Renewable and Sustainable Energy ARTICLE pubs.aip.org/aip/rse

Low-frequency wind speed variations and their impact on wind farm performance

Cite as: J. Renewable Sustainable Energy **18**, 043304 (2026); doi: 10.1063/5.0332176
Submitted: 2 March 2026 · Accepted: 17 June 2026 ·
Published Online: 4 August 2026

View Online Export Citation CrossMark

Yang Liu, Anja Stieren, and Richard J. A. M. Stevens[a)]

AFFILIATIONS

Physics of Fluids Group, Max Planck Center Twente for Complex Fluid Dynamics, J.M. Burgers Center for Fluid Dynamics, University of Twente, P.O. Box 217, 7500 AE Enschede, The Netherlands

[a)]Author to whom correspondence should be addressed: r.j.a.m.stevens@utwente.nl

ABSTRACT

Standalone large-eddy simulations (LES) of wind farms often assume steady inflow conditions, overlooking low-frequency, large-scale wind variabilities. As a result, they capture only higher-frequency boundary-layer turbulence and miss wind speed variations on timescales longer than several minutes. We demonstrate that the low-frequency wind speed variations significantly impact wind farm performance. We address this by incorporating dynamic wind speed changes in wind farm LES using a non-inertial moving reference frame within the concurrent precursor framework, allowing the simulation domain to follow mass-conserving, time-varying wind speed signals with minimal changes to standard setups. Simulations show that such variability can strongly influence wake flows and wind farm power output, with wake losses decreasing during flow acceleration and increasing during deceleration. These effects result from changes in wind speed on timescales significantly longer than the wake advection time between successive downstream turbines, which traditional LES do not resolve. Accounting for this variability will be important for improving wind farm performance predictions and for developing control strategies that are robust to changing inflow conditions.

I. INTRODUCTION

Large-eddy simulations (LES) are an important numerical tool to investigate the interactions between atmospheric turbulence and wind farms. By capturing three-dimensional flow structures and turbine wakes, LES provides detailed insights into energy generation, wake recovery, and structural loads on wind turbines. However, most wind farm LES assume idealized, statistically steady atmospheric boundary layer (ABL) conditions.[1–4] As a result, such simulations primarily resolve small-scale atmospheric turbulence with timescales shorter than a few minutes, while slower low-frequency variations are not represented. However, the growing scale of wind turbines and farms makes it increasingly important to account for the influence of large-scale, low-frequency atmospheric dynamics on wind farm performance.

In reality, the atmosphere is continually evolving as weather systems shift.[5–7] This drives relatively slow variations in wind speed and direction, which strongly affect turbine inflow conditions and wake meandering.[8] Large-scale atmospheric motions occur over hundreds of kilometers, far larger than a typical LES domain. Therefore, they cannot be resolved in wind farm LES. In contrast to atmospheric boundary-layer turbulence, which evolves over seconds to minutes, these large-scale, low-frequency variations typically span 15 min to several hours. They are commonly studied using mesoscale weather and climate models, where turbulence is fully parameterized. This mismatch between mesoscale modeling and turbulence-resolving wind farm LES creates a knowledge gap in how low-frequency variations influence wind farm flow physics, a regime often referred to as *terra incognita*.[9–11] Prior studies have shown that variations in wind direction can influence wind farm performance beyond what is predicted by averaging across different wind directions.[11–13] Experiments also show that unsteady inflow conditions can significantly modulate wind-turbine wake structures compared with steady-state inflow.[14,15] The impact of unsteady wake dynamics on wind farm performance and control, driven by low-frequency atmospheric variations, remains poorly understood due to the lack of simulation methods to study these effects under controlled conditions.[16] Therefore, it is essential to develop simulation approaches that allow controlled variation of low-frequency atmospheric conditions to advance our understanding of wind farm dynamics and evaluate control strategies.

Approaches for incorporating changing atmospheric conditions into LES involve coupling it with weather models, such as the Weather Research and Forecasting (WRF) model.[17–19] Two main strategies have been developed: (i) domain nesting, where LES is embedded within a coarser-scale weather simulation, and (ii) direct forcing of LES using output from the weather model.[11,12,20,21] While nesting captures large-scale variability, the lack of resolved turbulence in weather models requires long fetch regions for the LES to develop realistic turbulent flow within the LES domain.[22–24] Forcing-based approaches are simpler but depend on pressure gradient changes that only slowly affect wind speed, making it challenging to represent the full range of atmospheric turbulence.[25] Nevertheless, most methods typically seek to fully assimilate mesoscale profiles, forcing a trade-off between preserving the boundary-layer turbulence structure and accurately reproducing the prescribed wind-speed signal. This compromise limits their suitability for well-controlled, quantitative investigations of how low-frequency wind-speed variations affect the wind farm flow field.

This study introduces a method to directly incorporate low-frequency wind speed variations, on timescales of several minutes or longer, into wind farm LES. Our approach integrates a non-inertial moving reference frame with the concurrent precursor method[12,21] to conserve mass and consistently introduce low-frequency wind-speed variability into wind farm simulations. The method is validated against steady-state reference cases to confirm accuracy and consistency. The ability to prescribe user-defined wind speed variations makes this method particularly suited for studying wind farm performance under controlled conditions. We then use a measured wind speed time series $U(t)$ to assess how dynamic wind speed variations impact wind farm performance. Under dynamic wind speed variations, wake flows generated by wind turbines exhibit a strong historical effect that is not evident in steady-state wind conditions. Even at the same inflow wind speed, downstream turbine power output varies significantly with wind speed history, a factor not yet emphasized in wind energy research.

The paper begins with a description of the LES setup in Sec. II. Section III introduces the new method for incorporating dynamic wind speed variations, which is validated by idealized test cases in Sec. IV. In Sec. V, we show how measured low-frequency wind speed variations can be used to drive LES. Section VI illustrates how dynamic inflow shapes wake flow and affects wind farm performance. The paper concludes with a discussion and outlook in Sec. VII.

II. LES FRAMEWORK

To demonstrate the proposed method, we examine a simplified case of a neutrally stratified pressure-driven ABL. The governing equations for the LES are provided by

$$\partial_i \widetilde{u}_i = 0, \qquad \partial_t \widetilde{u}_i + \partial_j(\widetilde{u}_i \widetilde{u}_j) = -\partial_i \widetilde{p}^* - \partial_j \tau_{ij} - \frac{\partial_i p_\infty}{\rho} + f_i. \tag{1}$$

The tilde indicates the spatial filtering at the LES grid scale Δ, and $\widetilde{u}_i$ represents the filtered variables. The driving pressure gradient is given by $\partial_i p_\infty/\rho = -u_*^2/H$, where u_* is the friction velocity. The traceless part of the sub-grid scale tensor, $\tau_{ij} = \widetilde{u_i u_j} - \widetilde{u}_i \widetilde{u}_j$, is modeled using the anisotropic minimum dissipation model. The filtered modified pressure is defined as $\widetilde{p}^* = \widetilde{p} - p_\infty/\rho - \tau_{kk}/3$. The term f_i represents the turbine forces in the wind farm domain, which are modeled using an actuator disk approach.[26] Due to the high Reynolds numbers associated with atmospheric flows, viscous stresses are considered negligible.

At the top of the domain, a no-penetration condition and zero shear stress are applied, and periodicity is enforced in the horizontal (streamwise and spanwise) directions. At the surface, wall shear stress is modeled using Monin–Obukhov similarity theory, with a surface roughness length of $z_0 = 0.1$ m, representing flat grassland conditions. All simulation variables are non-dimensionalized using the domain height H and the reference friction velocity $u_*|_{t_0}$, resulting in a characteristic timescale $t_{\mathrm{ndim}} = H/u_*$. Horizontal spatial derivatives are computed with a pseudo-spectral method, while second-order central finite differences are used vertically. Time integration is performed using a third-order Adams–Bashforth scheme. Additional numerical details are available in Gadde *et al.*[27]

III. MODELING DYNAMICALLY CHANGING WIND SPEED IN LES

Figure 1 illustrates the conceptual idea of our approach, which is inspired by the work of Stieren *et al.*[12] on dynamic wind direction changes. We decompose the wind speed signal as $U(t) = U_s + U_d(t)$, where the stationary part $U_s = U(t_0)$ is the initial value of the signal at time t_0. The dynamic component $U_d(t)$ captures the temporal evolution of $U(t)$ relative to U_s. Starting from an equilibrium ABL with wind speed U_s, the dynamic part $U_d(t)$ is introduced by moving the non-inertial reference frame of the simulation domain in the opposite direction, such that the reference frame velocity is given by $U_{\mathrm{Frame}}(t) = -U_d(t)$. In the moving frame of reference, this results in an apparent force that drives the dynamic changes in wind speed.

The resulting momentum equation in Cartesian coordinates reads as

$$\partial_t \widetilde{u}_i + \partial_j(\widetilde{u}_i \widetilde{u}_j) = -\partial_i \widetilde{p}^* - \partial_j \tau_{ij} - \frac{\partial_i p_\infty}{\rho} + f_i + \dot{U}(t)\,\delta_{i1}, \tag{2}$$

where the time derivative $\dot{U}$ represents the inertial force arising from the translation of the reference frame. Since wind speed varies with height, the signal $U(t)$ is defined as a domain-averaged quantity. For simplicity, we consider only wind speed variations in the streamwise direction, as indicated by the Kronecker delta δ_{i1}. This approach builds upon, and can be combined with, the method for modeling dynamic wind direction changes by Stieren *et al.*.[12] We assume that the ABL remains in a quasi-equilibrium state during the dynamic process. Consequently, we update the friction velocity and adjust the mean pressure gradient $\partial_i p_\infty/\rho$ at each time step to match the evolving wind speed.

A key challenge in adjusting the incoming wind speed is maintaining mass conservation, as changes in part of the domain can disrupt the momentum flux across different cross sections.[25] We address this by integrating our method within the concurrent precursor framework for simulating wind farms in ABLs.[12,21] In this setup, two simulations run simultaneously: a precursor simulation alongside the actual wind farm simulation. At each time step, data sampled from the precursor are copied into the fringe region of the wind farm domain, where they serve as the inflow condition. The wind speed signal is applied throughout the domain in both the precursor and wind farm simulations. Specifically, mass conservation requires that the streamwise mass flux through any cross section normal to the mean-flow direction remains constant. By introducing a domain-uniform forcing via a moving reference frame, the present method enforces a horizontally uniform variation in wind speed that is consistent with

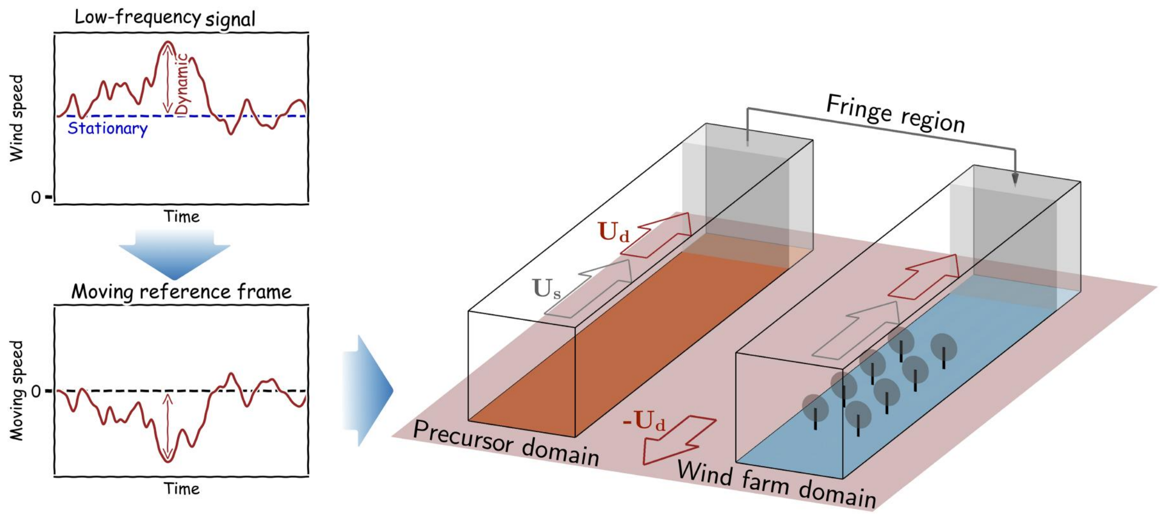

FIG. 1. Illustrations for modeling low-frequency wind speed variations in wind farm LES. The simulation begins with a stationary wind speed U_s, and the dynamic signal U_d is introduced by translating the simulation domain's reference frame in the opposite direction at the same speed.

this constraint. This enables low-frequency wind speed variations to be smoothly incorporated into the ABL turbulence resolved by LES.

IV. IDEALIZED TEST CASES

We begin by examining simplified monotonic wind speed variations to verify the proposed method. To this end, we perform neutral ABL simulations in a domain of size $12.56 \times 6.28 \times 1\,\text{km}^3$ in the streamwise, spanwise, and vertical directions, respectively, using a grid of $256 \times 128 \times 64$ points. Since the physical viscosity of air is ignored in Eq. (2), the simulation is fully non-dimensionalized using the length scale H and the friction velocity scale u_*. For illustrative purposes, we choose the non-dimensionalization parameters as $H_{\text{ndim}} = 1\,\text{km}$ and $u_{*,\text{ndim}} = 1\,\text{m/s}$, making each non-dimensional time unit equal to $t_{\text{ndim}} = H_{\text{ndim}}/u_{*,\text{ndim}} = 1000\,\text{s}$. A baseline simulation of a stationary ABL with $u_{*,\text{ref}} = u_{*,\text{ndim}}$ serves as a reference, with its domain-averaged streamwise velocity represented by U_{Ref}. For the acceleration scenario, a linear velocity increase from U_{Ref} to $2U_{\text{Ref}}$ is imposed over $\Delta t_{\text{ndim}} = 0.5$, 2, and 8 time units, corresponding to doubling the wind speed in approximately 8 min (fast), 30 min (medium), and 2 h (slow), respectively. Similarly, for the deceleration scenario, the wind speed decreases from $2U_{\text{Ref}}$ to U_{Ref}. The dynamic changes are initiated at $t_{\text{ndim}} = 50$ when the system is in the statistically stationary state.

Figure 2(a) shows the time evolution of the domain-averaged streamwise velocity. In all cases, the wind speed closely follows the imposed signal, confirming that the dynamic forcing is applied as intended. Figure 2(b) presents the vertical profile of streamwise velocity, averaged over both the acceleration and deceleration phases. The results confirm that the flow remains in quasi-equilibrium throughout the dynamic forcing. The normalized velocity profile, scaled by the

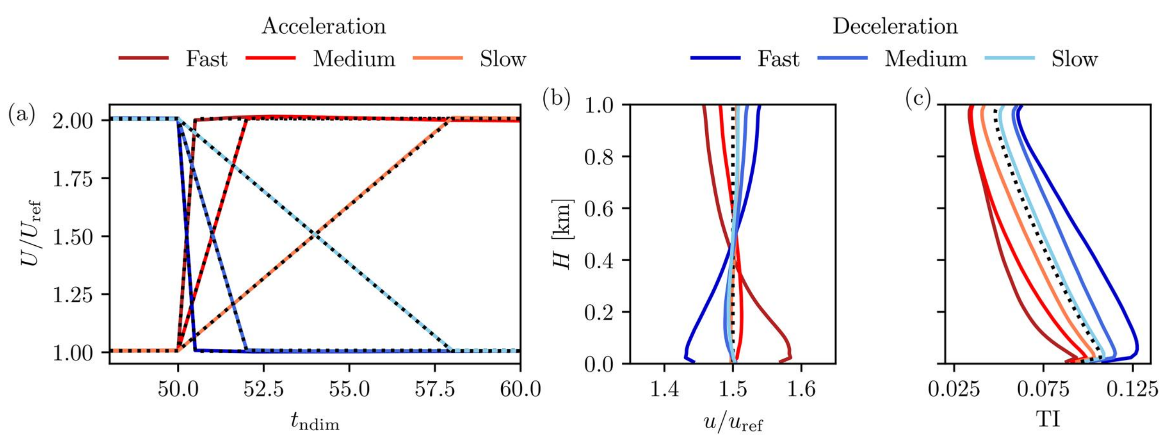

FIG. 2. (a) Time variation of normalized velocity; (b) vertical profile of streamwise velocity normalized by u_{ref}; and (c) vertical profile of turbulent intensity for idealized test cases. The dashed line in panel (a) indicates the imposed wind speed; in panels (b) and (c), it represents the equilibrium ABL profile. Note that U/U_{ref} in (a) denotes domain-averaged velocities. In contrast, u/u_{ref} and the turbulent intensity in (b) and (c) are height-dependent and averaged over time and the horizontal plane during the acceleration period.

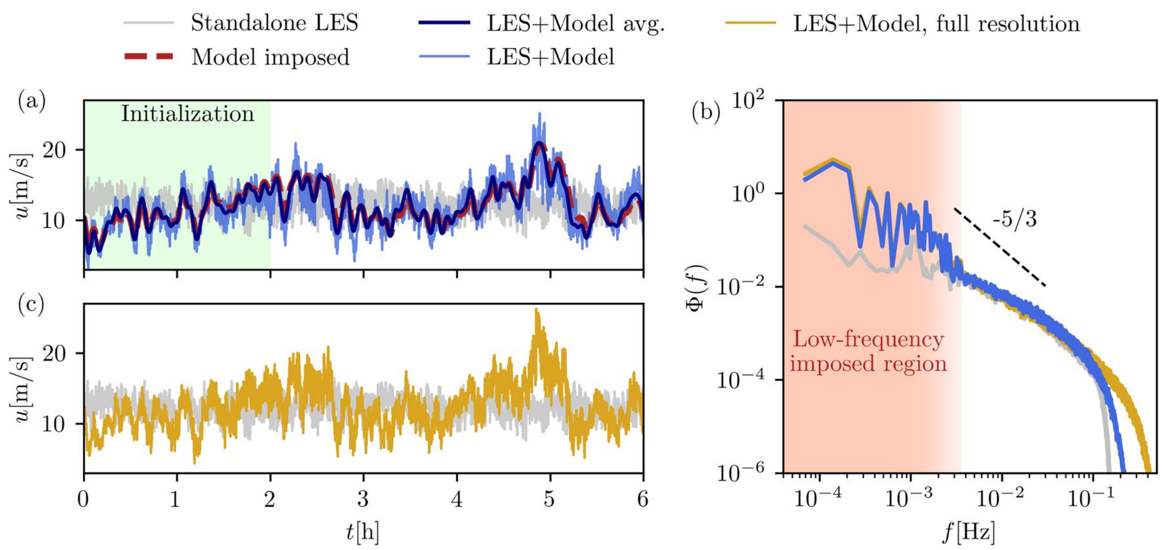

FIG. 3. Comparison between measured wind speed, standalone LES, and LES, including modeled low-frequency variations. (a) Time series, and (b) power spectrum. The "Model imposed" lines in (a) and (b) indicate the low-frequency signal in our model. Lines "LES+Model avg." and "LES+Model" represent the horizontally averaged and locally sampled wind speed signals, respectively. Panel (c) compares the "full resolution" simulation on a 512 × 256 × 128 grid with standalone LES.

reference profile u_{ref}, stays within 6% of the imposed value. Deviations are most noticeable near the surface, where the flow tends to overshoot, and at higher altitudes, where the velocity is slightly lower than the reference. This pattern is consistent with experimental observations of accelerating boundary layers.[28] The primary effect of flow acceleration is an imbalance between the driving pressure gradient and vertical momentum transport by turbulence. This imbalance arises from the delayed response of turbulent structures to changes in the mean wind speed.[29,30] As a result, wind speed variations influence turbulent fluctuations with a time lag, and the effect on turbulence intensity is more pronounced during rapid accelerations and decelerations. Figure 2(c) illustrates this behavior, showing that turbulence intensity decreases during acceleration and increases during deceleration.

V. LOW-FREQUENCY WIND SPEED VARIATIONS

To demonstrate our method's ability to replicate realistic wind-speed variations, we use a model signal derived from a field-measured wind-speed time series in our LES. The data were recorded on January 28, 2018, between 4:30 a.m. and 10:30 a.m. at a height of $z = 87$ m on the M5 meteorological mast at the NREL National Wind Technology Center.[31] This dataset was chosen based on two criteria: (i) the ABL remained approximately neutral throughout the period, with $|z/L| \leq 0.05$, and (ii) there were no significant changes in wind direction. To isolate the low-frequency components, we apply a low-pass filter with a cutoff frequency of $f_c = 1.8 \times 10^{-3}$ Hz to the original signal. To smoothly integrate it into the LES, we used a second-order Butterworth filter with a transition band extending up to $2f_c$, corresponding to timescales of approximately 5 min. The resulting signal, called "Model imposed", is shown in Fig. 3. To prevent transient effects, we treat the first 2 h as an initialization phase and use only the last 4 h of the 6-h data for quantitative analysis.

We use the same LES domain and grid setup as described in Sec. IV. Figure 3 shows that standalone LES without dynamic forcing lacks the low-frequency variations seen in atmospheric flows. The figure demonstrates that the horizontally averaged velocity from the LES with our model (LES+Model avg.) closely follows the imposed low-frequency wind speed variations (Model imposed). A closer look reveals a slight deviation from the target signal. This observation is consistent with Fig. 2(b), which shows that rapid accelerations can drive the vertical profile away from its equilibrium state, even though the domain-averaged wind speed follows the imposed signal. At $z = 87$ m, this manifests as a small overshoot in the wind-speed time series. However, we note that these overshoots are small compared to the high-frequency fluctuations visible in the locally sampled signals, see Figs. 3(a) and 3(b).

Figure 3(c) confirms a smooth spectral transition between the low-frequency signal imposed by our modeling approach and the high-frequency turbulence naturally captured by LES. The smooth transition is achieved through the Butterworth filter, which gradually adds low-frequency content (timescales longer than several minutes) to the standalone LES, which otherwise only captures turbulent fluctuations up to several minutes. We performed a higher resolution simulation (512 × 256 × 128 nodes, labeled "LES+Model, full resolution") to verify that the low-frequency content stays consistent in a higher resolution simulation. Meanwhile, the high-resolution simulation captures more high-frequency content, as expected, because the grid better resolves smaller length scales and higher-frequency turbulence events.

VI. EFFECT OF DYNAMIC WIND SPEED VARIATIONS ON WIND FARM PERFORMANCE

To examine how low-frequency wind speed fluctuations with typical time scales of more than several minutes influence wind farm performance, we simulate a wind farm with 28 DTU 10 MW wind

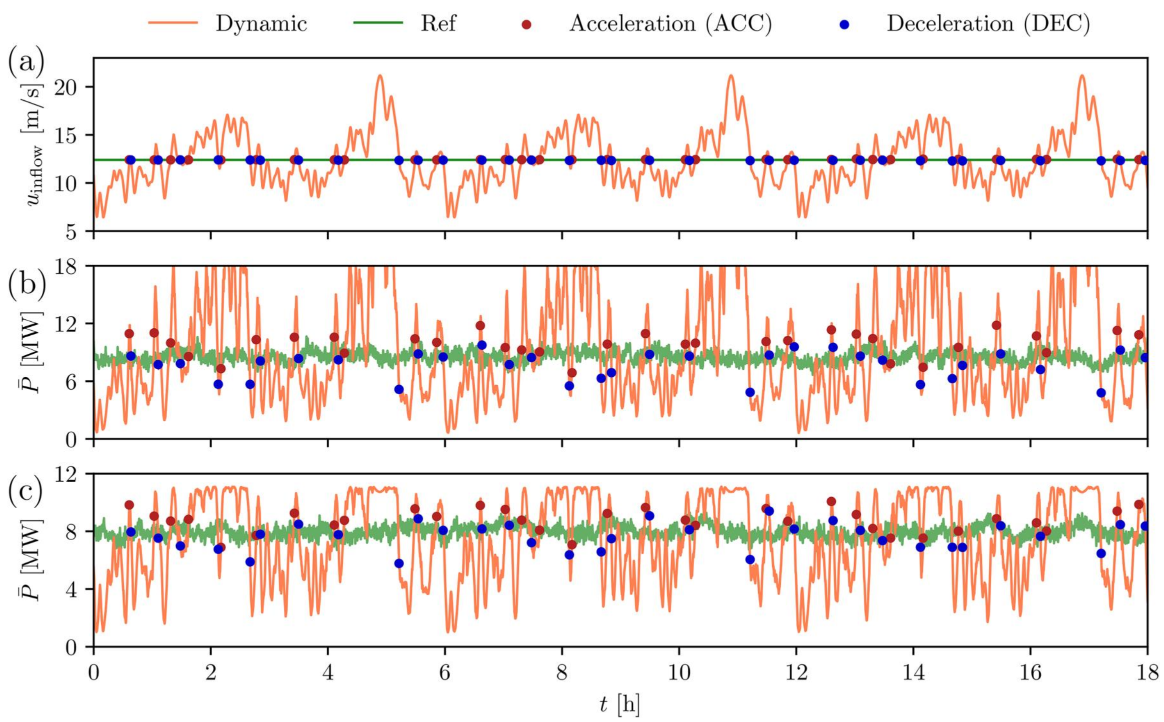

FIG. 4. (a) Imposed wind speed at hub height, (b) corresponding averaged turbine power production in the wind farm for $C_T = 0.8$ and (c) power production for dynamic C_T. The red (accelerating) and blue (decelerating) points indicate when the imposed dynamic wind speed matches the average wind speed (reference case). Note that the y axis in panel (b) is truncated to highlight the comparison with the reference case. Peak power values for the constant C_T case exceed the axis limit but are not central to the present analysis.

turbines.[32] The turbines are arranged in seven rows and four columns, with streamwise spacing of 7D and spanwise spacing of 5D. Simulation runs are conducted on a grid of $512 \times 256 \times 128$ points within a domain measuring $12.56 \times 6.28 \times 1\,\text{km}^3$. Each turbine, modeled with the actuator disk method, is resolved with seven grid points across its diameter, which is sufficient to capture the main interactions with the ABL.[26]

The dynamic case uses the low-pass filtered wind speed signal shown in Fig. 3(c) as inflow for 18 h by repeating a 6-h segment three times, see Fig. 4(a). The reference case uses a constant wind speed equal to the time-averaged value of the dynamic case. We compare these two cases to assess the effect of low-frequency wind-speed variations on wind farm power output. In Sec. VI A, we first consider an idealized academic case with a fixed turbine thrust coefficient of $C_T = 0.8$. Section VI B then presents a more realistic scenario where C_T varies dynamically according to the EllipSys power curve from Bak *et al.*[32], which specifies a maximum power of $P_{\text{max}} \approx 11$ MW.

A. Wind farm operating at constant C_T

We begin with the idealized scenario where all turbines operate at a constant thrust coefficient of $C_T = 0.8$, and the resulting wind farm power output over time is shown in Fig. 4(b). The figure highlights moments when the wind speed in the dynamic scenario matches the average wind speed from the reference case. These moments are categorized based on whether the flow is speeding up or slowing down. When the flow accelerates, the wind farm produces more power than in the reference case. Conversely, during deceleration, the power output is lower than in the reference case at the same inflow wind speed.

Figure 5(a) shows the power output normalized by the production of the first row. The results indicate that flow acceleration and deceleration mainly impact the performance of downstream rows. During acceleration, turbines in the second row and beyond generate more power than in the reference case. This relative increase comes from higher wind speeds starting at the second row, as shown in Fig. 5(b).

Notably, the differences in wind speed and turbulence intensity before reaching the wind farm remain small, see Figs. 5(b) and 5(c), suggesting that the observed changes arise from internal wake dynamics rather than ambient inflow. These results illustrate that dynamic wind speed variations can substantially affect wake development compared with the stationary conditions typically assumed in current studies.

For downstream rows, the higher inflow wind speed and lower turbulence intensity during acceleration, see Figs. 5(b) and 5(c), indicate mitigated wake impacts compared to decelerating conditions. This behavior indicates that the turbine wake dynamics depend on the history of varying wind-speed conditions. During acceleration, the upstream turbines operated at lower wind speeds in the preceding period and therefore produced weaker velocity deficits, since the extracted momentum scales with inflow wind speed ($u_\infty - u_{\text{disc}} \propto u_\infty$). Consequently, downstream turbines benefit

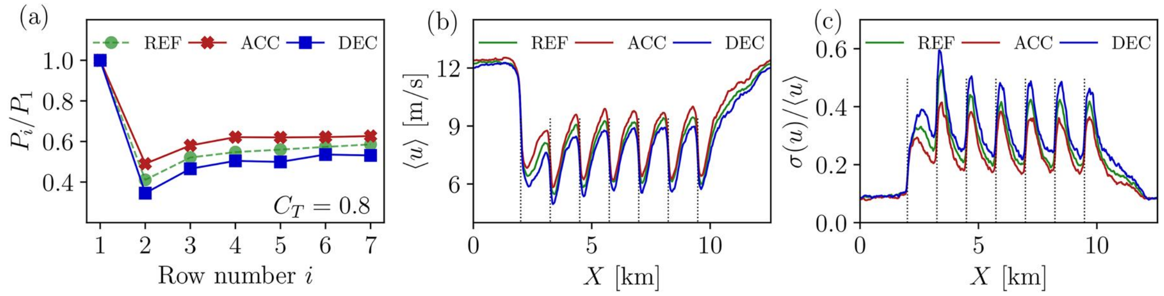

FIG. 5. Results for idealized scenario with turbines operating at constant $C_T = 0.8$. (a) Relative power output per row, (b) streamwise velocity, and (c) turbulence intensity as functions of downstream position for the acceleration, deceleration, and reference scenarios. Vertical dashed lines in panels (b) and (c) indicate turbine locations.

from more favorable inflow conditions due to these weaker velocity deficits generated in the past and produce more power than in the reference case. Conversely, in the deceleration scenario, higher past wind speeds generated stronger upstream wakes, which are carried downstream and reduce the power output of the following turbines.

The dynamic wake effects at time t, which influence downstream turbine performance, are mainly driven by prior wind speed changes, expressed as $\Delta U = U(t) - U(t - \Delta t)$, where $\Delta t = \Delta x/\bar{U}$ is the wake travel time between turbines. The effective wind speed $\bar{U}$ is the mean value of dynamic wind speed U over the time interval Δt. This highlights the role of low-frequency wind speed fluctuations, since the effects of higher-frequency changes tend to cancel within Δt due to alternating acceleration and deceleration. We define the transition frequency for this effect as $f_t = (2\Delta t)^{-1}$; for $f > f_t$, no sustained acceleration or deceleration occurs within Δt. To test whether wake travel time correlates with observed performance changes, we performed simulations incorporating wind speed variations at specific frequencies. The chosen frequencies follow the $f^{-5/3}$ spectral slope characteristic of atmospheric turbulence, see Fig. 6(a), as observed in the NREL field measurements. They span 10^{-4} to 10^{-2} Hz, corresponding to timescales from about 2.8 h to 1.7 min.

Figure 6(b) shows that below the transition frequency f_t, the power output during acceleration events is typically about 3%–5% higher than during deceleration. This difference is smaller than in Fig. 5(a), likely because the results in Fig. 6 consider the average of the entire acceleration and deceleration period, where the opposite effects are mixed in at the initial period. The transition frequency f_t corresponds to twice the average wake travel time between consecutive downstream turbines, which in our case is about 5×10^{-3} Hz (approximately 3 min). While lower frequencies represent slower wind-speed changes, their fluctuation amplitude increases with the spectral scaling $\Phi(f) \sim f^{-5/3}$. These opposing effects yield a persistent ΔU at low frequencies, producing a nearly constant power difference between acceleration and deceleration events in this range. For $f > f_t$, this difference vanishes as high-frequency fluctuations cancel over the wake travel time Δt due to alternating acceleration and deceleration.

B. Wind farm operating at dynamic C_T

Figure 4(c) shows the wind farm's power output, where the turbine thrust coefficient dynamically adjusts to the incoming wind speed following the EllipSys power curve.[32] Peak power production occurs at an inflow velocity of approximately $u_{\text{inflow}} = 15$ m/s, as this allows turbines operating in wake conditions to consistently reach rated power. This produces an asymmetry in the turbine power response to the incoming wind flow.

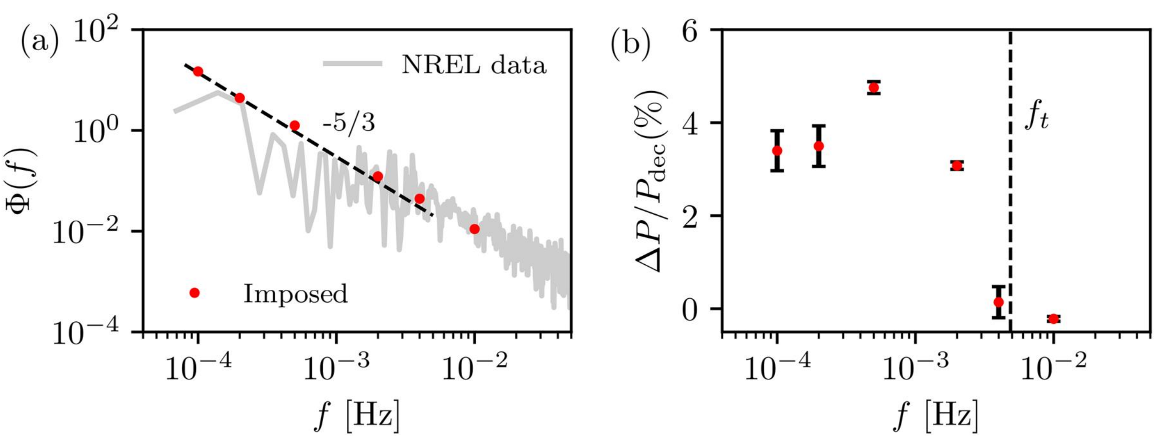

FIG. 6. Frequency-dependent power asymmetry for idealized scenario with turbines operating at constant $C_T = 0.8$. (a) Imposed mono-frequency wind speed variations with amplitudes following a $f^{-5/3}$ spectral scaling, representative of atmospheric turbulence. (b) Average power difference between acceleration and deceleration periods, showing a consistent gain in power production during acceleration at low frequencies.

Figure 7(a) shows the power output normalized by the first row's production. While the overall trends resemble those in the constant C_T case, some differences are apparent, particularly for the second row. Also, Figs. 7(b) and 7(c) show that, immediately behind the first turbine row, the acceleration case exhibits lower wind speed and higher turbulence intensity, a trend opposite to that observed farther downstream. This can be explained by the operating regime of the first-row turbines, which frequently exceed rated wind speed, see Fig. 7(b). In the above-rated regime, the thrust coefficient C_T decreases with increasing wind speed. Consequently, during acceleration, the upstream turbines experienced lower wind speeds in the past and therefore operated at higher C_T, producing stronger momentum extraction and a larger wake deficit. This enhanced deficit can offset the wake-mitigation effect expected from increasing wind speed.

In the deceleration scenario, the above-rated upstream turbines experienced higher wind speeds in the past and thus operated at lower C_T. The reduced thrust implies weaker momentum extraction and a weaker wake deficit, which offset the stronger wakes that would otherwise be expected as the wind speed decreases. Because for both accelerating and decelerating conditions, the variation of C_T for the above-rated operation counteracts the trend induced by wind-speed variations, the wind-speed deficit differences among scenarios are much smaller directly behind the first row than farther downstream, and the corresponding power differences are also small. The net outcome depends on the interplay between two competing mechanisms: the direct effect of the changing inflow velocity on wake recovery and the history-dependent variation of C_T, which modifies the momentum extraction by the upstream turbines. The relative importance of these mechanisms depends on the turbine control strategy governing C_T.

It is important to note that the power differences shown in Fig. 7 depend on the specific characteristics of the wind speed signal and on the wind speed level selected for comparison. The magnitude of the acceleration and deceleration effects can vary with the chosen analysis intervals. For example, Fig. 7(a) shows an asymmetric response relative to the reference case, with the normalized power output during deceleration more closely matching the reference than during acceleration. Examination of Fig. 7(b) indicates that this is because the downstream wind speed during deceleration is closer to the reference than during acceleration. As seen in Fig. 4(a), most deceleration events occur immediately after acceleration phases, causing the effects to partially overlap.

Considering the aggregate power output over the entire time period in Fig. 4(c), the wind farm produces less power under dynamic wind inflow (orange line) than in the corresponding reference scenario (green line). Under stationary inflow at the mean wind speed, see Fig. 4(c), production is near maximum capacity. In high-wind periods, turbines reach maximum output quickly, so gains are small, while in low-wind periods, production drops sharply, reducing overall output. In contrast, for the idealized constant thrust coefficient scenario with $C_T = 0.8$, dynamic inflow yields a power gain. This results from the cubic dependence of power on inflow velocity ($P \sim U_\infty^3$), where gains during high-wind periods outweigh losses during low-wind periods. Overall, these effects are scenario-specific and depend on turbine design and control. While a full exploration of all cases is beyond the scope of this work, the proposed method enables such investigations under controlled conditions.

VII. CONCLUSIONS

We present a method for incorporating low-frequency wind-speed variations into large-eddy simulations (LES) of wind farms. Traditional standalone LES often miss these dynamics because they arise from large-scale atmospheric processes, whereas most studies assume steady inflow. Our approach introduces low-frequency fluctuations by dynamically adjusting the velocity of a non-inertial reference frame. When combined with the concurrent precursor method, it preserves mass conservation, which is often challenging when modifying inflow conditions in turbulence simulations. The implementation is straightforward and validated through multiple test cases that reproduce both idealized and field-measured low-frequency wind-speed variations within the LES, ensuring smooth transitions to the high-frequency turbulence resolved by the LES. The method requires only one modification to an existing LES solver. The inertial forcing term $-\dot{U}(t)$ is added to the right-hand side of the momentum equation. Since $\dot{U}$ is spatially uniform, no additional stencil operations, Poisson solves, filtering, or parallel communications are needed, and the additional wall-clock time was less than 0.5% of the overall computational cost. The spatial discretization, pressure solver, turbine model, and parallelization strategy are all left unchanged, making the method directly applicable to large wind farm and long-duration atmospheric boundary-layer simulations. This capability enables controlled, systematic investigations of how low-frequency fluctuations affect wind farm performance and control.

The results show that low-frequency variations in wind speed can significantly affect wind farm performance. When the wind accelerates, downstream turbines experience reduced wake losses, whereas during slowdowns, wake effects are stronger. These effects are controlled by the

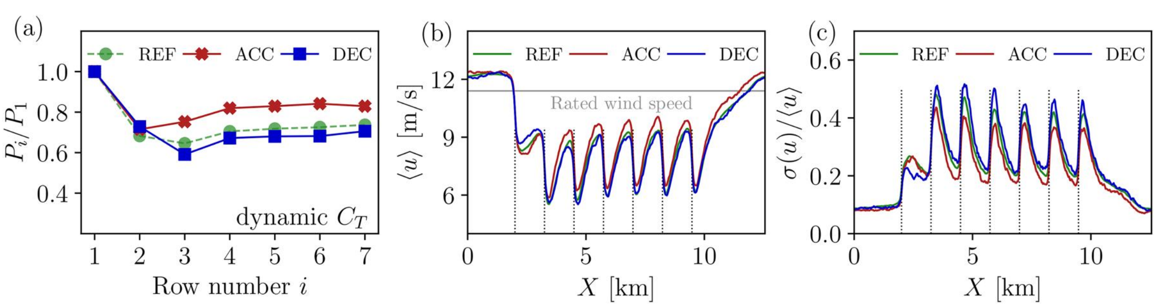

FIG. 7. Results for turbines operating according to DTU 10 MW power curve. (a) Relative power output per row, (b) streamwise velocity, and (c) turbulence intensity as functions of downstream position for the acceleration, deceleration, and reference scenarios. Vertical dashed lines in panels (b) and (c) indicate turbine locations.

advection time for wakes to travel between successive downstream turbines and disappear when wind speed fluctuations occur on shorter timescales. Because standalone LES do not resolve low-frequency dynamics, they must be modeled explicitly, as done in this study. Results also differ between turbines operating at a fixed thrust coefficient and those following a realistic power curve, highlighting the role of turbine-response dynamics. This scenario dependence arises from the asymmetric, nonlinear response of turbines to changing inflow, as both the thrust coefficient and wake evolution depend on wind speed and turbulence intensity. We therefore expect these effects to vary with atmospheric stability and wind farm layout.

The present study applies the approach to wind-speed variations under neutral atmospheric conditions. The framework itself, however, is not restricted to neutral boundary layers, as the inertial forcing term can be added alongside buoyancy, Coriolis, surface-model, and mesoscale-forcing terms without altering the basic numerical formulation, discretization, or solver structure, making the method directly extendable to more realistic atmospheric regimes, including LES driven by outputs from large-scale weather models or measurement data.[5,6] In such applications, however, the quantitative conclusions on the impact of low-frequency wind-speed variations on wind farm power output may change because stability, terrain heterogeneity, and mesoscale forcing introduce additional dynamics, including changes in turbulence intensity, boundary-layer depth, wake recovery, wind direction, and pressure gradient forcing.[12] Among these, stable stratification deserves particular attention, as slow turbulence recovery may challenge the assumption that turbulence remains close to equilibrium during the imposed dynamic process, potentially affecting the accuracy of the reproduced wind profiles. These aspects require further investigation beyond the scope of the present work. Future work could also prescribe variations in geostrophic wind speed rather than near-surface velocity, which may better represent large-scale atmospheric dynamics.

ACKNOWLEDGMENTS

This project has received funding from the European Research Council (ERC) under the European Union's Horizon Europe research and innovation program (Grant Agreement No. 101124815). This work was carried out on the Dutch national e-infrastructure with support from the SURF Cooperative. The authors gratefully acknowledge the Gauss Center for Supercomputing e.V. (www.gauss-centre.eu) for funding this project by providing computing time on the GCS Supercomputer Super-MUC-NG at Leibniz Supercomputing Center (www.lrz.de).

AUTHOR DECLARATIONS

Conflict of Interest

The authors have no conflicts to disclose.

Author Contributions

Yang Liu: Conceptualization (equal); Data curation (equal); Investigation (lead); Methodology (lead); Validation (lead); Writing – original draft (equal); Writing – review & editing (equal). **Anja Stieren:** Conceptualization (supporting); Investigation (supporting); Methodology (supporting); Supervision (equal); Validation (equal). **Richard J. A. M. Stevens:** Conceptualization (equal); Data curation (equal); Funding acquisition (equal); Investigation (equal); Methodology (equal); Project administration (equal); Supervision (equal); Validation (equal); Writing – original draft (equal); Writing – review & editing (equal).

DATA AVAILABILITY

The data that support the findings of this study are available from the corresponding author upon reasonable request.

REFERENCES

[1] R. J. A. M. Stevens and C. Meneveau, "Flow structure and turbulence in wind farms," Annu. Rev. Fluid Mech. **49**, 311–339 (2017).

[2] P. Veers, K. Dykes, E. Lantz, S. Barth, C. L. Bottasso, O. Carlson, A. Clifton, J. Green, P. Green, H. Holttinen, D. Laird, V. Lehtomäki, J. K. Lundquist, J. Manwell, M. Marquis, C. Meneveau, P. Moriarty, X. Munduate, M. Muskulus, J. Naughton, L. Pao, J. Paquette, J. Peinke, A. Robertson, J. S. Rodrigo, A. M. Sempreviva, J. C. Smith, A. Tuohy, and R. Wiser, "Grand challenges in the science of wind energy," Science **366**, eaau2027 (2019).

[3] F. Porté-Agel, M. Bastankhah, and S. Shamsoddin, "Wind-turbine and wind-farm flows: A review," Boundary-Layer Meteorol. **174**, 1–59 (2020).

[4] P. Veers, K. Dykes, S. Basu, A. Bianchini, A. Clifton, P. Green, H. Holttinen, L. Kitzing, B. Kosović, J. K. Lundquist, J. Meyers, M. O'Malley, W. J. Shaw, and B. Straw, "Grand challenges: Wind energy research needs for a global energy transition," Wind Energy Sci. **7**, 2491–2496 (2022).

[5] S. E. Haupt, B. Kosović, W. Shaw, L. K. Berg, M. Churchfield, J. Cline, C. Draxl, B. Ennis, E. Koo, R. Kotamarthi, L. Mazzaro, J. Mirocha, P. Moriarty, D. Muñoz-Esparza, E. Quon, R. K. Rai, M. Robinson, and G. Sever, "On bridging a modeling scale gap: Mesoscale to microscale coupling for wind energy," Bull. Am. Meteorol. Soc. **100**, 2533–2550 (2019).

[6] S. E. Haupt, B. Kosović, L. K. Berg, C. M. Kaul, M. Churchfield, J. Mirocha, D. Allaerts, T. Brummet, S. Davis, A. DeCastro, S. Dettling, C. Draxl, D. J. Gagne, P. Hawbecker, P. Jha, T. Juliano, W. Lassman, E. Quon, R. K. Rai, M. Robinson, W. Shaw, and R. Thedin, "Lessons learned in coupling atmospheric models across scales for onshore and offshore wind energy," Wind Energy Science **8**, 1251–1275 (2023).

[7] B. Kosović, S. Basu, J. Berg, L. K. Berg, S. E. Haupt, X. G. Larsén, J. Peinke, R. J. A. M. Stevens, P. Veers, and S. Watson, "Impact of atmospheric turbulence on performance and loads of wind turbines: knowledge gaps and research challenges," Wind Energy Science **11**, 509–555 (2026).

[8] A. H. Syed and J. Mann, "Simulating low-frequency wind fluctuations," Wind Energy Sci. **9**, 1381–1391 (2024).

[9] J. C. Wyngaard, "Toward numerical modeling in the 'Terra Incognita'," J. Atmos. Sci. **61**, 1816–1826 (2004).

[10] K. Rai, L. K. Berg, B. Kosović, S. E. Haupt, J. D. Mirocha, B. L. Ennis, and C. Draxl, "Evaluation of the impact of horizontal grid spacing in terra incognita on coupled mesoscale–microscale simulations using the WRF framework," Mon. Weather Rev. **147**, 1007–1027 (2019).

[11] W. Munters, C. Meneveau, and J. Meyers, "Turbulent inflow precursor method with time-varying direction for large-eddy simulations and applications to wind farms," Boundary-Layer Meteorol. **159**, 305–328 (2016).

[12] A. Stieren, S. N. Gadde, and R. J. A. M. Stevens, "Modeling dynamic wind direction changes in large eddy simulations of wind farms," Renewable Energy **170**, 1342–1352 (2021).

[13] B. Foloppe, W. Munters, S. Buckingham, L. Vandevelde, and J. van Beeck, "Development of a dynamic wake model accounting for wake advection delays and mesoscale wind transients," J. Phys. Conf. Ser. **2265**, 022055 (2022).

[14] N. J. Wei, A. El Makdah, J. Hu, F. Kaiser, D. E. Rival, and J. O. Dabiri, "Wake dynamics of wind turbines in unsteady streamwise flow conditions," J. Fluid Mech. **1000**, A66 (2024).

[15] T. Messmer, J. Peinke, A. Croce, and M. Hölling, "The role of motion-excited coherent structures in improved wake recovery of a floating wind turbine," J. Fluid Mech. **1018**, A23 (2025).

[16] J. Meyers, C. Bottasso, K. Dykes, P. A. Fleming, P. Gebraad, G. Giebel, T. Göçmen, and J.-W. van Wingerden, "Wind farm flow control: Prospects and challenges," Wind Energy Sci. **7**, 2271–2306 (2022).

[17] W. C. Skamarock, J. B. Klemp, J. Dudhia, D. O. Gill, D. M. Barker, M. G. Duda, X. Y. Huang, W. Wang, and J. G. Powers, "A description of the advanced research WRF version 3," NCAR Technical Note No. NCAR/TN-475+STR (National Center for Atmospheric Research, 2008), pp. 1–126.

[18] D. Allaerts, E. Quon, C. Draxl, and M. Churchfield, "Development of a time–height profile assimilation technique for large-eddy simulation," Boundary-Layer Meteorol. **176**, 329–348 (2020).

[19] R. S. Arthur, J. D. Mirocha, N. Marjanovic, B. D. Hirth, J. L. Schroeder, S. Wharton, and F. K. Chow, "Multi-scale simulation of wind farm performance during a frontal passage," Atmosphere **11**, 245 (2020).

[20] T. Chatterjee, N. W. Cherukuru, Y. Peet, and R. J. Calhoun, "Large eddy simulation with realistic geophysical inflow of Alpha Ventus wind farm: A comparison with LIDAR field experiments," J. Phys.: Conf. Ser. **1037**, 072056 (2018).

[21] R. J. A. M. Stevens, J. Graham, and C. Meneveau, "A concurrent precursor inflow method for large eddy simulations and applications to finite length wind farms," Renewable Energy **68**, 46–50 (2014).

[22] D. Muñoz-Esparza and B. Kosović, "Generation of inflow turbulence in large-eddy simulations of nonneutral atmospheric boundary layers with the cell perturbation method," Mon. Weather Rev. **146**, 1889–1909 (2018).

[23] F. K. Chow, C. Schär, N. Ban, K. A. Lundquist, L. Schlemmer, and X. Shi, "Crossing multiple gray zones in the transition from mesoscale to microscale simulation over complex terrain," Atmosphere **10**, 274 (2019).

[24] S. E. Haupt, L. Berg, M. Churchfield, B. Kosović, J. Mirocha, and W. Shaw, "Mesoscale to microscale coupling for wind energy applications: Addressing the challenges," J. Phys.: Conf. Ser. **1452**, 012076 (2020).

[25] S. Andersen, N. Sørensen, and M. Kelly, "LES modelling of highly transient wind speed ramps in wind farms," J. Phys.: Conf. Ser. **1934**, 012015 (2021).

[26] R. J. A. M. Stevens, L. A. Martínez-Tossas, and C. Meneveau, "Comparison of wind farm large eddy simulations using actuator disk and actuator line models with wind tunnel experiments," Renewable Energy **116**, 470–478 (2018).

[27] S. N. Gadde, A. Stieren, and R. J. A. M. Stevens, "Large-eddy simulations of stratified atmospheric boundary layers: Comparison of different subgrid models," Boundary-Layer Meteorol. **178**, 363–382 (2021).

[28] H. Fernholz and D. Warnack, "The effects of a favourable pressure gradient and of the Reynolds number on an incompressible axisymmetric turbulent boundary layer. Part 1. The turbulent boundary layer," J. Fluid Mech. **359**, 329–356 (1998).

[29] S. He and J. Jackson, "A study of turbulence under conditions of transient flow in a pipe," J. Fluid Mech. **408**, 1–38 (2000).

[30] D. Greenblatt and E. A. Moss, "Rapid temporal acceleration of a turbulent pipe flow," J. Fluid Mech. **514**, 65–75 (2004).

[31] NWTC Information Portal, see https://nwtc.nrel.gov/135mData for "NWTC 135-m meteorological towers data repository" (2026); accessed: 22 February 2026.

[32] C. Bak, F. Zahle, R. Bitsche, T. Kim, A. Yde, L. C. Henriksen, M. H. Hansen, J. P. A. A. Blasques, M. Gaunaa, and A. Natarajan, "The DTU 10-MW reference wind turbine," in Danish Wind Power Research 2013, 2013.